Front. Energy 2019, 13(3): 450–463
https://doi.org/10.1007/s11708-018-0569-8

RESEARCH ARTICLE

Haizheng DANG, Dingli BAO, Zhiqian GAO, Tao ZHANG, Jun TAN, Rui ZHA, Jiaqi LI, Ning LI, Yongjiang ZHAO, Bangjian ZHAO

Theoretical modeling and experimental verifications of the single-compressor-driven three-stage Stirling-type pulse tube cryocooler

Abstract This paper establishes a theoretical model of the single-compressor-driven (SCD) three-stage Stirling-type pulse tube cryocooler (SPTC) and conducts experimental verifications. The main differences between the SCD type and the multi-compressor-driven (MCD) crycooler are analyzed, such as the distribution of the input acoustic power in each stage and the optimization of the operating parameters, in which both advantages and difficulties of the former are stressed. The effects of the dynamic temperatures are considered to improve the accuracy of the simulation at very low temperatures, and a specific simulation example aiming at 10 K is given in which quantitative analyses are provided. A SCD three-stage SPTC is developed based on the theoretical analyses and with a total input acoustic power of 371.58 W, which reaches a no-load temperature of 8.82 K and can simultaneously achieve the cooling capacities of 2.4 W at 70 K, 0.17 W at 25 K, and 0.05 W at 10 K. The performance of the SCD three-stage SPTC is slightly poorer than that of its MCD counterpart developed in the same laboratory, but the advantages of lightweight and compactness make the former more attractive to practical applications.

Keywords single-compressor-driven, three-stage, Stirling-type pulse tube cryocooler, theoretical modeling, experimental verification

Received Feb. 10, 2018; accepted Apr. 16, 2018; online Jul. 20, 2018

Haizheng DANG (✉), Jun TAN, Ning LI
State Key Laboratory of Infrared Physics, Shanghai Institute of Technical Physics, Chinese Academy of Sciences, Shanghai 200083, China
E-mail: haizheng.dang@mail.sitp.ac.cn

Dingli BAO, Tao ZHANG, Rui ZHA, Jiaqi LI, Yongjiang ZHAO, Bangjian ZHAO
State Key Laboratory of Infrared Physics, Shanghai Institute of Technical Physics, Chinese Academy of Sciences, Shanghai 200083, China; University of Chinese Academy of Sciences, Beijing 100049, China

Zhiqian GAO
Institute of Fundamental and Frontier Technology, Midea Refrigerator Co., Ltd., Hefei 230601, China

1 Introduction

The pulse tube cryocooler (PTC) is now widely acknowledged as a significant technological innovation in the regenerative cooling technology because it completely eliminates the moving component at the cold end [1–2]. The Stirling-type PTC (SPTC) which is driven by the linear compressor based on the well-proven principles of clearance seal and flexure springs realizes the long life of the driver at the warm end, and thus has a strong appeal to many special application fields such as in space [1–2]. A practical SPTC usually needs a three-stage arrangement to achieve an effective cooling capacity at 10 K or below. Generally, there are two typical coupling approaches for the cold fingers of a three-stage SPTC, namely, the gas-coupled [3] and the thermally-coupled [4–8], in which the latter is simple in structure and easy to control the internal flow, while the former is more compact and potentially has a higher efficiency because the thermal links are avoided. In practice, many thermally-coupled three-stage cold fingers might also actually adopt the mixed coupling approach, in which the first two stages are gas-coupled while the last stage is thermally coupled to the former [4–8]. The completely gas-coupled three-stage SPTC is driven by a single compressor, while a thermally-coupled or mixed-coupled counterpart could be driven by either multiple compressors or a single-compressor. A multi-compressor-driven (MCD) thermally-coupled multi-stage SPTC is much easier to design because it can actually be regarded as multiple single-stage SPTCs linked by the thermal links. However, obviously, a single-compressor-driven (SCD) multi-stage counterpart is desirable in practical applications because of its lighter weight and simpler system.

However, the design and optimization of a SCD multi-stage SPTC has to face many difficulties because, normally, the working temperature of each stage varies substantially, which results in considerable differences on the properties of both the working gas and the matrix, especially at very low temperatures. In contrast, a single compressor means that the charge pressure, the pressure ratio, and especially the operating frequency have to be kept the same for each stage. As a result, a SCD design has to take all stages into consideration and many compromises also have to be made in order to avoid the huge irreversible losses, which is one of the main reasons why many designers have to resort to the MCD approach. Some experimental progresses have been made in SCD three-stage SPTCs, either thermally-coupled or mixed-coupled, but most of them focuses on the structural design, practical manufacture, and performance optimization, whereas the detailed theoretical analyses of the working mechanism have seldom been conducted. Recently the same authors [9] have established a theoretical model of the MCD thermally-coupled three-stage SPTC based on the entropy analysis and quantitatively analyzed the irreversible losses and the effects of parameters. Based on the previous work, this paper will further establish the theoretical model of the SCD one. Several approaches to analyzing single-stage and multi-stage SPTCs or M-type PTCs are also used for valuable references [10–15]. In the developed model, the effects of dynamic temperature will be considered and the distribution of the input acoustic power in each stage will be analyzed in-depth. Moreover, different matrices will be discussed at very low temperatures and the operational parameters such as the charge pressure, the pressure ratio, and the frequency will be optimized as well. Furthermore, verification experiments will be conducted and experimental results will be compared with those of the MCD three-stage SPTC developed in the same laboratory.

2 Establishment of the model

Figure 1 shows the schematic of the three-stage SPTC driven by a single compressor with a total input acoustic power of W. The acoustic power flows into the three-stage after coolers and becomes W_1, W_2, and W_3, respectively:

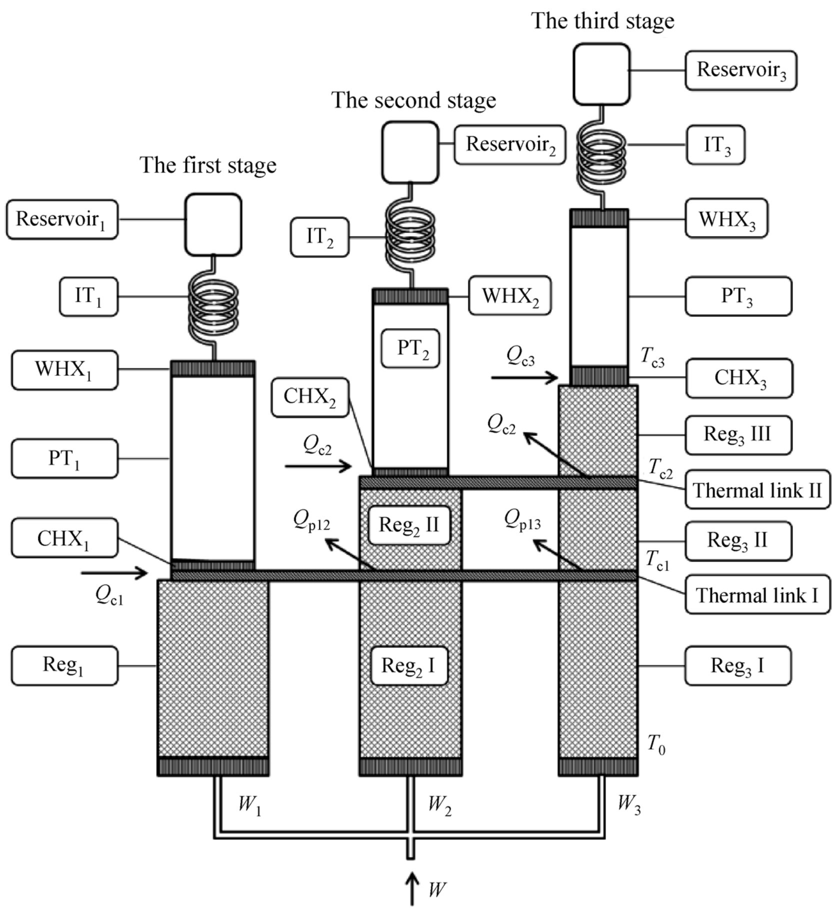

Fig. 1 Schematic of the SCD three-stage SPTC

$$W = W_1 + W_2 + W_3. \tag{1}$$

According to the Second Law of Thermodynamics, the cooling capacity of each stage of the SPTC can be expressed as [9]

$$Q_{g1} = \frac{T_{c1}}{T_0}\left(W_1 - <\dot{H}_{h1}> - Q_{ah1}\right) - T_{c1} <\dot{S}_{g1}>, \tag{2}$$

$$Q_{g2} = \frac{T_{c2}}{T_0}\left(W_2 - <\dot{H}_{h2}> - Q_{ah2}\right)$$
$$+\eta_{12}\cdot\frac{T_{c2}}{T_{c1}}Q_{p12} - T_{c2} <\dot{S}_{g2}>, \tag{3}$$

$$Q_{g3} = \frac{T_{c3}}{T_0}\left(W_3 - <\dot{H}_{h3}> - Q_{ah3}\right) + \eta_{13}\cdot\frac{T_{c3}}{T_{c1}}Q_{p13}$$
$$+\eta_2\cdot\frac{T_{c3}}{T_{c2}}Q_{p2} - T_{c3} <\dot{S}_{g3}>, \tag{4}$$

where Q_g is the gross cooling capacity of each stage, Q_p is the precooling capacity, Q_{ah} is the axial heat conduction at the hot end of each regenerator, η is the heat conduction efficiency of the thermal link, T_c is the cooling temperature, $<\dot{H}_h>$ is the time-average enthalpy flow rate at the hot end of each regenerator, $<\dot{S}_g>$ is the time-average entropy generation rate in each stage, and the subscripts 1, 2, and 3 represent the three stage cryocoolers, respectively.

The entropy generations are caused by the irreversible losses in regenerators and heat exchangers, which mainly consist of the axial heat conduction S_a, the pressure drop S_p, and the ineffective heat convection between the gas and the matrix S_c. The three kinds of entropy generations have been analyzed quantitatively according to Ref. [9], the temperature profiles in the three regenerators and the heat exchanging in both the regenerators and the heat exchangers have been discussed as well.

$$\mathrm{d} <\dot{S}_a> = (\lambda_w A_w + \lambda_i A_i)\frac{1}{T^2}\left(\frac{\partial T}{\partial x}\right)^2 \mathrm{d}x, \tag{5}$$

$$\mathrm{d} <\dot{S}_p>$$
$$= -\frac{C_f R\rho}{2p_s}|\dot{U}|\left[\mathrm{d}|\boldsymbol{p}_d|\cos\Delta\theta + |\boldsymbol{p}_d|\mathrm{d}\theta_p\cos\left(\Delta\theta + \frac{\pi}{2}\right)\right], \tag{6}$$

$$\mathrm{d} <\dot{S}_c> = \frac{\mathrm{d}Q_{gs}}{T_s} - \frac{\mathrm{d}Q_{gs}}{T_g} \approx \frac{(\mathrm{d}Q_{gs})^2}{h_{gs}T^2\mathrm{d}A_{gs}}, \tag{7}$$

where λ_w and λ_i are the thermal conductivities of the wall and inner part of the matrix; A_w and A_i are the corresponding cross sectional areas, respectively; C_f is the compressibility factor, $|\boldsymbol{p}_d|$ and θ_p are the amplitude and phase angle of the dynamic pressure, respectively; $|\dot{\boldsymbol{U}}|$ is the amplitude of the volume flow rate; $\Delta\theta$ is the phase difference between the dynamic pressure and the volume flow rate; Q_{gs} is the heat exchanging between the solid and the gas; A_{gs} is the heat transfer area; h_{gs} is the convective heat transfer coefficient; and T_s and T_g are the temperatures of the solid and the gas, respectively, which oscillate during a cycle.

2.1 Dynamic temperatures of the gas and the matrix

According to Eqs. (5)–(7), in order to obtain the entropy generations in the regenerators and the heat exchangers, the accurate values of the dynamic pressure and the volume flow rate at any position of the SPTC have to be found out. The usual approach to solve this problem is to employ the electrical circuit analogy (ECA) models [16–17]. However, the models mentioned above consider the interactions between the volume flow rate and the dynamic pressure but neglect the influence of the dynamic temperature, which could be acceptable at above about 40 K but may result in a noticeable inaccuracy at very low temperatures, for instance, in the third stage of the SPTC. Therefore, herein a further improved ECA model will be developed by taking the dynamic temperature into account.

According to the momentum equation of the gas, when both the dynamic pressure $\boldsymbol{p}_d$ and the volume flow rate $\dot{\boldsymbol{U}}$ are assumed to be harmonic, there is

$$\Delta\boldsymbol{p}_d = -\frac{\mathrm{i}\omega\rho_m\Delta x/A}{1-(1-i)\delta_v/2r_h}\dot{\boldsymbol{U}}$$
$$\cong -\left(\frac{i\omega\rho_m\Delta x}{A} + R_v\right)\dot{\boldsymbol{U}}, \tag{8}$$

where ω is the angular frequency, δ_v is the viscous penetration depth, R_v is the viscous resistance, r_h is the hydraulic radius, and the bold words represent vectors.

The regenerators and pulse tubes in the SPTC can be regarded as adiabatic, thus the continuity equation of the gas can be expressed as

$$\boldsymbol{p}_d = -\frac{\gamma_m p_m}{i\omega A\Delta x}\Delta\dot{\boldsymbol{U}} + \frac{p_m \ln p_m}{\gamma_m}\left(\frac{\partial\gamma}{\partial p}\boldsymbol{p}_d + \frac{\partial\gamma}{\partial T}T_g\right). \tag{9}$$

In after coolers, hot and cold heat exchangers, inertance tubes, and reservoirs, the thermodynamic processes are all isothermal, thus the continuity equation becomes

$$\boldsymbol{p}_d = -\frac{p_m}{i\omega A\Delta x}\Delta\dot{\boldsymbol{U}} + \frac{p_m}{C_{fm}}\left(\frac{\partial C_f}{\partial p}\boldsymbol{p}_d + \frac{\partial C_f}{\partial T}T_g\right), \tag{10}$$

where T_g is the dynamic temperature of the gas, γ is the specific heat ratio, and the subscript m stands for the mean value of each parameter.

In the regenerators, the heat convection between the gas and the wall are neglected due to the adiabatic thermodynamic process. Therefore, the energy conservation equation for the matrix is

$$\mathrm{d}Q_{\mathrm{gs}} = h_{\mathrm{gs}}\left(T_{\mathrm{g}} - T_{\mathrm{s}}\right)\mathrm{d}A_{\mathrm{gs}} = c_{\mathrm{s}}\rho_{\mathrm{s}}A_{\mathrm{i}}(1-\phi)\frac{\partial T_{\mathrm{s}}}{\partial t}\mathrm{d}x. \tag{11}$$

And for the gas

$$\mathrm{d}Q_{\mathrm{gs}} = \left(c_{\mathrm{g}}\rho_{\mathrm{g}}A_{\mathrm{i}}\varphi\frac{\partial T_{\mathrm{g}}}{\partial t} + c_{\mathrm{g}}\rho_{\mathrm{g}}A_{\mathrm{i}}\varphi u\frac{\partial T_{\mathrm{g}}}{\partial x} - A_{\mathrm{i}}\varphi\frac{\partial p}{\partial t}\right)\mathrm{d}x, \tag{12}$$

where φ is the porosity and u is the velocity of the gas.

Combing Eqs. (11) and (12), when both T_{g} and T_{s} are assumed to be harmonic, the amplitudes and phase angles of the two dynamic temperatures can be worked out as

$$|T_{\mathrm{g}}| = \sqrt{\frac{\phi^2|\boldsymbol{p}_{\mathrm{d}}|^2 + 2F\phi|\boldsymbol{p}_{\mathrm{d}}|\sin\Delta\theta + F^2}{c_{\mathrm{g}}^2\rho_{\mathrm{g}}^2\phi^2 - 2c_{\mathrm{g}}\rho_{\mathrm{g}}\phi c_{\mathrm{s}}\rho_{\mathrm{s}}(1-\phi)\cos\theta_{\mathrm{gs}}/E + c_{\mathrm{s}}^2\rho_{\mathrm{s}}^2(1-\phi)^2/E^2}}, \tag{13}$$

$$\theta_{\mathrm{g}} = \theta_{\mathrm{p}} + \arctan\frac{F\cos\Delta\theta}{\phi|p_{\mathrm{d}}| + F\sin\Delta\theta} - \arctan\frac{c_{\mathrm{s}}\rho_{\mathrm{s}}(1-\phi)\sin\theta_{\mathrm{gs}}}{Ec_{\mathrm{g}}\rho_{\mathrm{g}}\phi - c_{\mathrm{s}}\rho_{\mathrm{s}}(1-\phi)\cos\theta_{\mathrm{gs}}}, \tag{14}$$

$$|T_{\mathrm{s}}| = \frac{1}{E}|T_{\mathrm{g}}|, \tag{15}$$

$$\theta_{\mathrm{s}} = \theta_{\mathrm{g}} - \theta_{\mathrm{gs}} = \theta_{\mathrm{g}} - \arctan\frac{\omega c_{\mathrm{s}}\rho_{\mathrm{s}}(1-\phi)}{\beta h_{\mathrm{gs}}}, \tag{16}$$

where β is the specific surface area in the regenerator, and E and F are defined as

$$E = \frac{|T_{\mathrm{g}}|}{|T_{\mathrm{s}}|} = \sqrt{1 + \left[\frac{\omega c_{\mathrm{s}}\rho_{\mathrm{s}}(1-\phi)}{\beta h_{\mathrm{gs}}}\right]^2}, \tag{17}$$

$$F = \frac{c_{\mathrm{g}}\rho_{\mathrm{g}}\phi|\dot{\boldsymbol{U}}|}{A_{\mathrm{i}}\omega}\frac{\partial T}{\partial x}. \tag{18}$$

To explain the dynamic temperature of the gas and the matrix discussed above, a specific example aiming at 10 K is given as follows. The main geometries of the three-stage SPTC are listed in Table 1. In the second stage, the relative position where thermal link 1 connects to the regenerator is 0.4 and the positive direction is defined from the after cooler to the cold heat exchanger. Similarly, in the third stage, the relative positions where thermal link 1 and thermal link 2 connect to the regenerator are 0.45 and 0.7, respectively.

Figure 2 demonstrates the distributions of $|\boldsymbol{p}_{\mathrm{d}}|$ and $|\dot{\boldsymbol{U}}|$ in the third regenerator when T_{g} is considered and ignored, respectively. The simulation results indicate that the effect of T_{g} is negligible when the temperature is above 70 K. Besides, in the temperature range of 70 K–25 K, the evident difference can be observed in both $|\boldsymbol{p}_{\mathrm{d}}|$ and $|\dot{\boldsymbol{U}}|$ when T_{g} is treated differently. However, when the temperature is below 25 K, T_{g} has a significant influence on both $|\boldsymbol{p}_{\mathrm{d}}|$ and $|\dot{\boldsymbol{U}}|$. According to Eq. (9), the specific heat ratio γ is almost constant when the temperature is above 70 K, thus the term $\partial\gamma/\partial T$ is near to zero. But when the temperature is below 25 K, the gas presents obvious non-ideal properties, and γ changes sharply with the temperature, which makes the influence of T_{g} non-negligible.

Figure 3 depicts the variations of $|T_{\mathrm{g}}|$, $|T_{\mathrm{s}}|$, θ_{g}, and θ_{s} with the relative position in the first regenerator. It should be noted that both $|T_{\mathrm{g}}|$ and $|T_{\mathrm{s}}|$ increase monotonically with the increasing relative position, although the temperature decreases along the regenerator. The above phenomenon is mainly caused by the monotonically decrease of the term $c_{\mathrm{s}}\rho_{\mathrm{s}}(1-\varphi)$ according to Eq. (13). In the first regenerator, $c_{\mathrm{s}}\rho_{\mathrm{s}}(1-\varphi)$ is much larger than $c_{\mathrm{g}}\rho_{\mathrm{g}}\varphi$, which means that the heat volumetric capacity of the matrix is much larger than that of the gas. In addition, as shown in Fig. 3, for the phase angles, both θ_{g} and θ_{s} first increase then decrease, and the phase difference between them, i.e., θ_{gs}, decreases monotonically due to the decreasing $c_{\mathrm{s}}\rho_{\mathrm{s}}(1-\varphi)$ according to Eq. (16).

Figures 4 and 5 display the variations of $|T_{\mathrm{g}}|$, $|T_{\mathrm{s}}|$, θ_{g},

Table 1 Main geometrical parameters of the SCD three-stage SPTC

		The first stage	The second stage	The third stage
Regenerator	Diameter	Φ30.3 mm × 0.2 mm	Φ24.8 mm × 0.2 mm	Φ19.5 mm × 0.2 mm
	Length	55.0 mm	76.4 mm	98.2 mm
	Matrix	#400 SS	40% #400 SS + 60% Lead	45% #400 SS + 25% Lead + 30% Er_3Ni
Hot heat exchanger	Diameter	30.3 mm	24.8 mm	19.5 mm
	Length	15.2 mm	13.2 mm	10.8 mm
Cold heat exchanger	Diameter	30.3 mm	24.8 mm	19.5 mm
	Length	7.3 mm	6.7 mm	5.1 mm

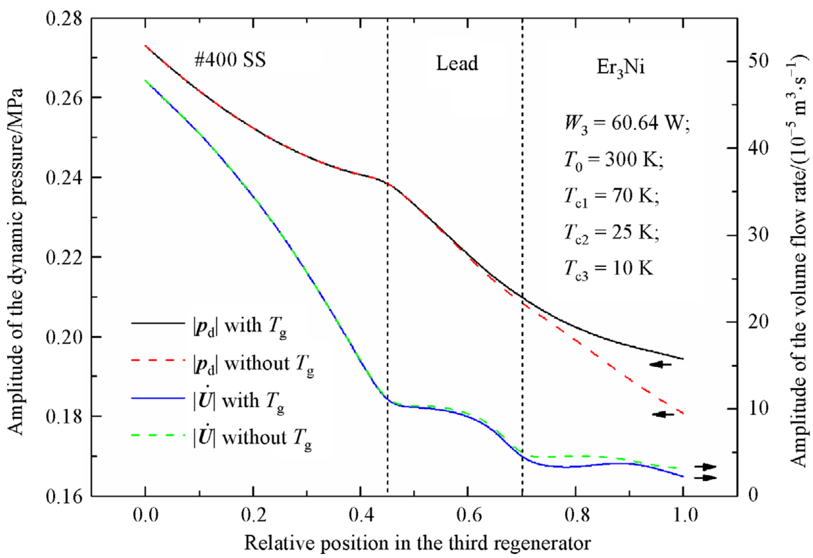

Fig. 2 Influence of T_g on $|\boldsymbol{p}_d|$ and $|\dot{\boldsymbol{U}}|$ in the third regenerator

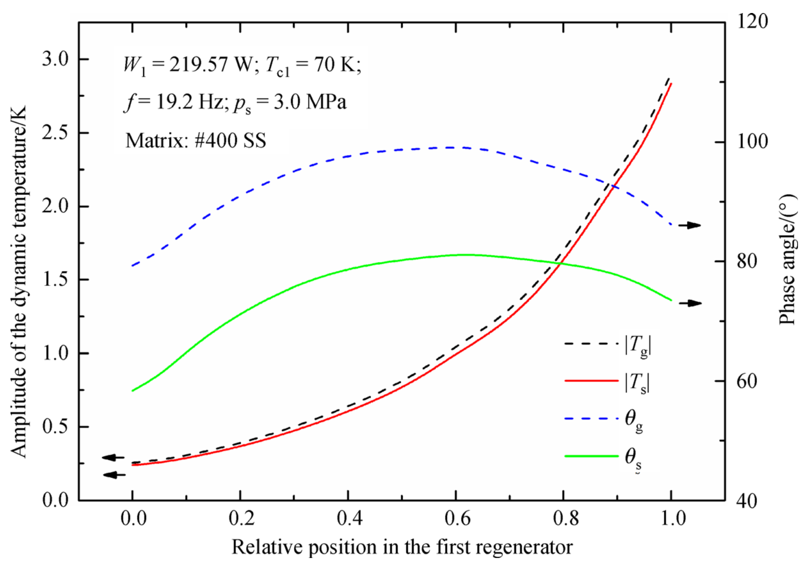

Fig. 3 Distributions of $|T_g|$, $|T_s|$, θ_g, and θ_s in the first regenerator

and θ_s with the relative position in the second and third regenerators, respectively. The abrupt changes of $|T_g|$, $|T_s|$, θ_g, and θ_s happen in both stages due to the layered structure of the matrix. For both $|T_g|$ and $|T_s|$, the amplitudes increase monotonically in both ranges of 300–70 K and 70–25 K, but between 10 K and 25 K, both $|T_g|$ and $|T_s|$ first increase and then decrease. The main reason for the above phenomena is that $c_s\rho_s(1-\varphi)$ decreases monotonically with the decreasing temperature in the regenerators, while $c_g\rho_g\varphi$ increases contrarily. In both ranges of 300–70 K and 70–25 K, $c_s\rho_s(1-\varphi)$ is much larger than $c_g\rho_g\varphi$, but between 10 K and 25 K, $c_g\rho_g\varphi$ increases sharply to the same order of magnitude with $c_s\rho_s(1-\varphi)$, and even becomes larger than the latter. Therefore, both $|T_g|$ and $|T_s|$ are mainly affected by the matrix at first, but the gas becomes predominant below about 20 K. In addition, the phase difference between θ_g and θ_s decreases monotonically in the whole temperature range from 300 to 10 K due to the continuous decreasing $c_s\rho_s(1-\varphi)$.

2.2 Distribution of the input acoustic power

Compared with the MCD three-stage SPTC model reported in Ref. [9], the SCD counterpart model in the present paper should lay more emphasis on the distribution of the input acoustic power in each stage. When the total input acoustic power is constant, according to Eqs. (8)–(10), the dynamic pressure $\boldsymbol{p}_{di}$, and the volume flow rate $\dot{U}_i$, at the inlet of each stage of the SPTC can be respectively expressed as [16–17],

$$\boldsymbol{p}_{\mathrm{di}}=\boldsymbol{p}_{\mathrm{de}}+\int_{\mathrm{ine}}\left(\frac{\omega\rho i}{A_{\mathrm{ine}}}+\frac{\mu\Pi_{\mathrm{ine}}}{A_{\mathrm{ine}}^{2}\delta_{\mathrm{v}}}\right)\dot{\boldsymbol{U}}_{x}\mathrm{d}x+\int_{\mathrm{hhx}}\left(\frac{\omega\rho i}{\phi_{\mathrm{hhx}}A_{\mathrm{hhx}}}+r_{\mathrm{g}}\right)\dot{\boldsymbol{U}}_{x}\mathrm{d}x+\int_{\mathrm{chx}}\left(\frac{\omega\rho i}{\phi_{\mathrm{chx}}A_{\mathrm{chx}}}+r_{\mathrm{g}}\right)\dot{\boldsymbol{U}}_{x}\mathrm{d}x$$
$$+\int_{\mathrm{reg}}\left(\frac{\omega\rho i}{\phi_{\mathrm{reg}}A_{\mathrm{reg}}}+r_{\mathrm{g}}\right)\dot{\boldsymbol{U}}_{x}\mathrm{d}x+\int_{\mathrm{aft}}\left(\frac{\omega\rho i}{\phi_{\mathrm{aft}}A_{\mathrm{aft}}}+r\right)_{\mathrm{g}}\dot{\boldsymbol{U}}_{x}\mathrm{d}x, \tag{19}$$

$$\dot{\boldsymbol{U}}_{\mathrm{i}}=\dot{\boldsymbol{U}}_{\mathrm{e}}+\int_{\mathrm{res}}\left(\frac{\omega A_{\mathrm{res}}i}{p_{\mathrm{m}}}\boldsymbol{p}_{\mathrm{dx}}\right)\mathrm{d}x+\int_{\mathrm{ine}}\left(\frac{\omega A_{\mathrm{ine}}i}{p_{\mathrm{m}}}\boldsymbol{p}_{\mathrm{dx}}\right)\mathrm{d}x+\int_{\mathrm{hhx}}\left[\frac{i\omega\phi_{\mathrm{hhx}}A_{\mathrm{hhx}}}{p_{\mathrm{m}}}\boldsymbol{p}_{\mathrm{dx}}-\frac{i\omega\phi_{\mathrm{hhx}}A_{\mathrm{hhx}}}{C_{\mathrm{fm}}}\left(\frac{\partial C_{\mathrm{f}}}{\partial p}\boldsymbol{p}_{\mathrm{dx}}+\frac{\partial C_{\mathrm{f}}}{\partial T}T_{\mathrm{gx}}\right)\right]\mathrm{d}x$$
$$+\int_{\mathrm{pul}}\left[\frac{i\omega A_{\mathrm{pul}}}{\gamma_{\mathrm{m}}p_{\mathrm{m}}}\boldsymbol{p}_{\mathrm{dx}}-\frac{i\omega A_{\mathrm{pul}}\ln p_{\mathrm{m}}}{\gamma_{\mathrm{m}}^{2}}\left(\frac{\partial\gamma}{\partial p}\boldsymbol{p}_{\mathrm{dx}}+\frac{\partial\gamma}{\partial T}T_{\mathrm{gx}}\right)\right]\mathrm{d}x+\int_{\mathrm{chx}}\left[\frac{i\omega\phi_{\mathrm{chx}}A_{\mathrm{chx}}}{p_{\mathrm{m}}}\boldsymbol{p}_{\mathrm{dx}}-\frac{i\omega\phi_{\mathrm{chx}}A_{\mathrm{chx}}}{C_{\mathrm{fm}}}\left(\frac{\partial C_{f}}{\partial p}\boldsymbol{p}_{\mathrm{dx}}+\frac{\partial C_{\mathrm{f}}}{\partial T}T_{\mathrm{gx}}\right)\right]\mathrm{d}x$$
$$+\int_{\mathrm{reg}}\left[\frac{i\omega\phi_{\mathrm{reg}}A_{\mathrm{reg}}}{\gamma_{\mathrm{m}}p_{\mathrm{m}}}\boldsymbol{p}_{\mathrm{dx}}-\frac{i\omega\phi_{\mathrm{reg}}A_{\mathrm{reg}}\ln p_{\mathrm{m}}}{\gamma_{\mathrm{m}}^{2}}\left(\frac{\partial\gamma}{\partial p}\boldsymbol{p}_{\mathrm{dx}}+\frac{\partial\gamma}{\partial T}T_{\mathrm{gx}}\right)+g\dot{\boldsymbol{U}}_{x}\right]\mathrm{d}x$$
$$+\int_{\mathrm{aft}}\left[\frac{i\omega\phi_{\mathrm{aft}}A_{\mathrm{aft}}}{p_{\mathrm{m}}}\boldsymbol{p}_{\mathrm{dx}}-\frac{i\omega\phi_{\mathrm{aft}}A_{\mathrm{aft}}}{C_{\mathrm{fm}}}\left(\frac{\partial C_{\mathrm{f}}}{\partial p}\boldsymbol{p}_{\mathrm{dx}}+\frac{\partial C_{\mathrm{f}}}{\partial T}T_{\mathrm{gx}}\right)\right]\mathrm{d}x, \tag{20}$$

where p_{de} and $\dot{U}_{\mathrm{e}}$ are the dynamic pressure and the volume flow rate at the end of the reservoir in each stage of the SPTC, respectively; A is the cross-sectional area of a component; φ is the porosity; and the subscripts "res, ine, hhx, pul, chx, reg, and aft" represent the components of reservoir, inertance tube, hot heat exchanger, pulse tube, cold heat exchanger, regenerator and after cooler in each stage of the SPTC, respectively. The positive direction in each stage is defined as from the after cooler to the reservoir.

The porosity in heat exchangers can be expressed as

$$\phi=\frac{A_{\mathrm{g}}}{A_{\mathrm{g}}+A_{\mathrm{s}}}, \tag{21}$$

where A_{g} and A_{s} are the cross-sectional areas of the gas and the solid, respectively.

In a SPTC, the reservoir is the last component which has only one inlet without any outlet. Therefore, the volume flow rate at the end of the reservoir is zero.

$$\dot{\boldsymbol{U}}_{\mathrm{e}1}=\dot{\boldsymbol{U}}_{\mathrm{e}2}=\dot{\boldsymbol{U}}_{\mathrm{e}3}=0. \tag{22}$$

And for the dynamic pressure at the inlet of each stage,

$$\boldsymbol{p}_{\mathrm{di}1}=\boldsymbol{p}_{\mathrm{di}2}=\boldsymbol{p}_{\mathrm{di}3}. \tag{23}$$

Combining Eqs. (19)–(23), p_{di} and $\dot{U}_{\mathrm{i}}$ in each stage can be worked out, and the input acoustic power can be written as

$$W_1=\frac{1}{2}\frac{RT_0\rho}{p_{\mathrm{s}}}\dot{\boldsymbol{U}}_{\mathrm{i}1}\boldsymbol{p}_{\mathrm{di}1}, \tag{24}$$

$$W_2=\frac{1}{2}\frac{RT_0\rho}{p_{\mathrm{s}}}\dot{\boldsymbol{U}}_{\mathrm{i}2}\boldsymbol{p}_{\mathrm{di}2}, \tag{25}$$

$$W_3=\frac{1}{2}\frac{RT_0\rho}{p_{\mathrm{s}}}\dot{\boldsymbol{U}}_{\mathrm{i}3}\boldsymbol{p}_{\mathrm{di}3}. \tag{26}$$

Table 2 Dynamic pressure and volume flow rate at the inlet of each stage

	The first stage	The second stage	The third stage	Total
$\lvert\dot{U}_{\mathrm{i}}\rvert/(\times 10^{-4}\ \mathrm{m^3/s})$	11.26	7.37	5.27	23.61
θui/(°)	9.76	23.16	31.28	18.63
$\lvert\boldsymbol{p}_{\mathrm{di}}\rvert$/kPa	273	273	273	273
θ_{pi}/(°)	0	0	0	0
$\Delta\theta_{\mathrm{i}}$/(°)	–9.76	–23.16	–31.28	–18.63
W/W	219.57	91.37	60.64	371.58

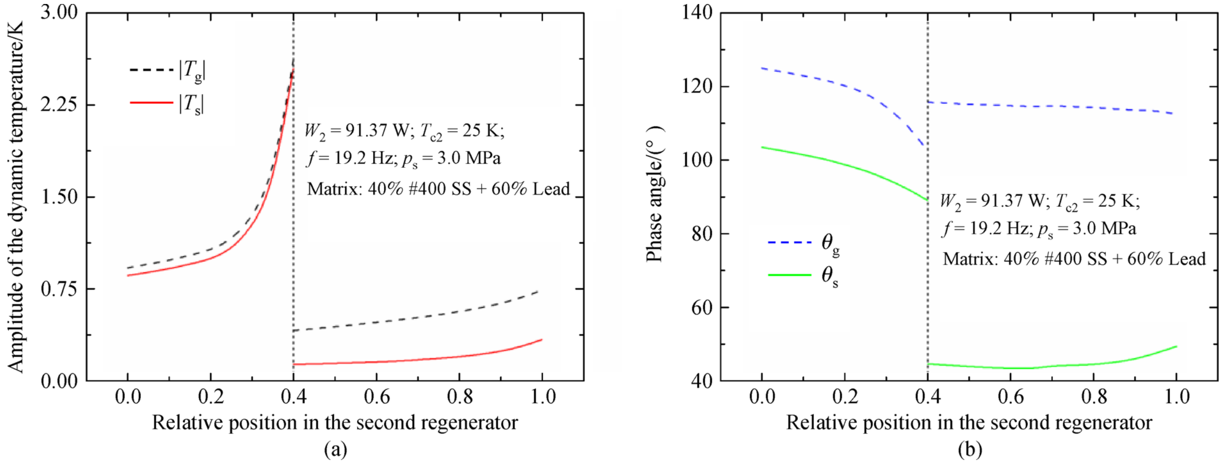

Fig. 4 Distributions of (a) $|T_g|$ and $|T_s|$, and (b) θ_g and θ_s in the second regenerator

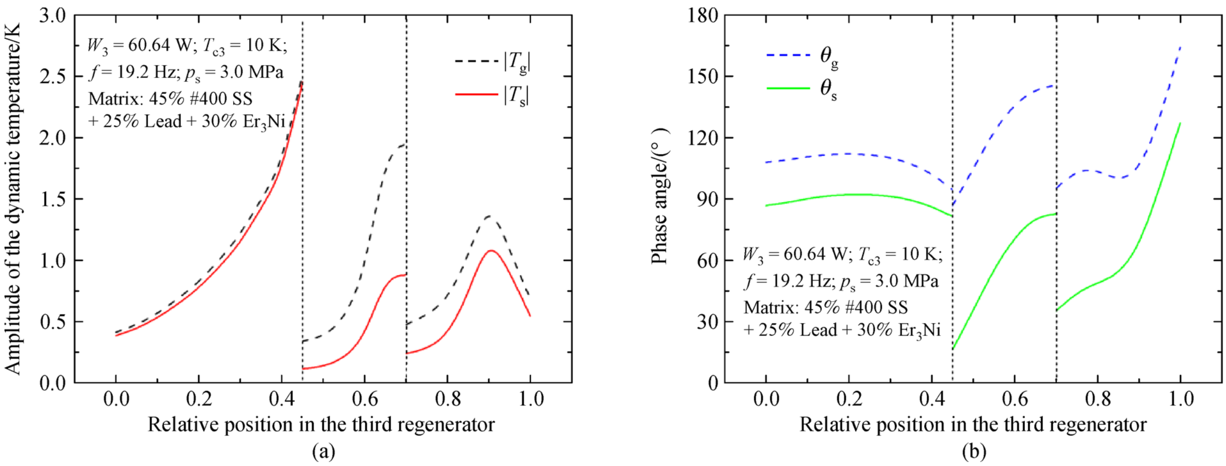

Fig. 5 Distributions of (a) $|T_g|$ and $|T_s|$, and (b) θ_g and θ_s in the third regenerator

For the example mentioned in Subsection 2.1, when the geometries of relevant components are fixed, the operating parameters at the inlet of each stage can be worked out quantitatively, and the detailed results are given in Table 2 with the charge pressure of 3.0 MPa and a frequency of 19.2 Hz. Generally, for the lower stage, the regenerator is longer and thinner, which may result in a larger resistance, and the input acoustic power is normally smaller than that of the upper stages.

3 Optimizations and discussion

Based on the above analyses, the performance of the SCD three-stage SPTC can be worked out quantitatively. Besides, it is found that the efficiency of the SCD three-stage SPTC is affected by a lot of parameters including the matrix, charge pressure, pressure ratio, operating frequency, etc. The optimizations on these parameters will be conducted as follows.

3.1 Effects of matrix in the third regenerator

Generally, the heat capacity of the matrix decreases monotonically with the decreasing temperature. Especially at a very low temperature, the heat capacity of some conventional matrix such as the stainless steel is even lower than that of the working fluid, which substantially reduces the regenerator efficiency. Therefore, the selection of the matrix is important especially in the regenerator of the last stage. For the above-mentioned example, the regenerator of the third stage is filled with 45% #400 SS and 25% Pb in the ranges of 300–70 K and 70–25 K, respectively. Moreover, in the range of 10–25 K, several rare-earth materials including Er_3Ni, ErNi, Pb, and $HoCu_2$ are investigated individually. The diameter of the rare-earth is 100 μm.

Figure 6 exhibits the temperature profiles of the third

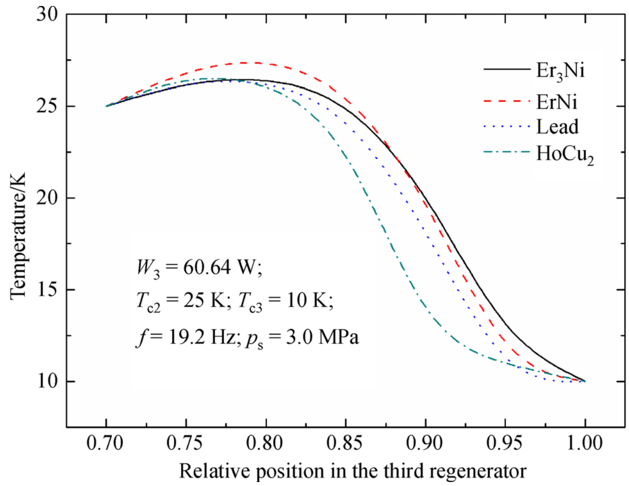

Fig. 6 Temperature profiles between 10 K and 25 K in the third regenerator with different matrices

regenerator in the temperature range of 25–10 K when the above different regenerator matrix is used, respectively. All of the four temperature profiles present obviously non-linear properties in the regenerator due to the non-ideal properties of the gas.

Figure 7 shows the influences of the different matrices on $|T_g|$ and $|T_s|$, between the relative positions of 0.7–1.0 in the third regenerator. The results indicate that both $|T_g|$ and $|T_s|$ first increase and then decrease with the increasing relative position because of the variations of $c_s\rho_s(1-\varphi)$ and $c_g\rho_g\varphi$ discussed in Subsection 2.1. In addition, the largest $|T_g|$ and $|T_s|$ occur when $HoCu_2$ is used, followed by ErNi and Pb, while Er_3Ni results in the smallest $|T_g|$ and $|T_s|$.

Figure 8 shows the effects of different matrices on $<\dot{S}_a>$, $<\dot{S}_p>$, $<\dot{S}_c>$, and $<\dot{S}_g>$ between 10 K and 25 K, respectively. $<\dot{S}_a>$, $<\dot{S}_p>$, $<\dot{S}_c>$, and $<\dot{S}_g>$ represent the entropy generation rates caused by axial heat conduction, pressure drop, ineffective heat convection, and the total irreversible losses in the third regenerator, respectively. The axial heat conduction caused by Pb is much larger than the other three materials due to its largest thermal conductivity, while the smallest axial heat conduction is caused by Er_3Ni. $HoCu_2$ produces the largest pressure drop, followed by ErNi, Pb, and Er_3Ni in proper order. Combining Eqs. (7) and (11), $<\dot{S}_c>$ is in proportion to $|T_s|^2$, and thus the variations of $<\dot{S}_c>$ for different matrices is the same which that of $HoCu_2$ is the largest while that of Er_3Ni is the smallest. According to the variation tendency of $<\dot{S}_a>$, $<\dot{S}_p>$, and $<\dot{S}_c>$, the total entropy generation rate $<\dot{S}_g>$, is the largest for $HoCu_2$, followed by Pb, ErNi, and Er_3Ni in sequence, and the cooling capacities at 10 K for them are 0.05 W, 0.08 W, 0.11 W, and 0.13 W, respectively. Thus Er_3Ni turns out to be the best choice for the given temperature range.

3.2 Effects of charge pressure and pressure ratio

For a MCD three-stage SPTC, the charge pressure and the pressure ratio of each stage can be optimized separately, and the efficiency of each stage can thus be maximized at the same time. In contrast, for a SCD three-stage SPTC, the charge pressure and the pressure ratio remain the same at the inlet of each stage according to Eq. (23). Therefore, the optimizations of the above two parameters should take into consideration their influence on all of the three stages simultaneously. Accordingly, a total cooling capacity Q_t, is defined as

$$Q_t = \frac{T_{c3}}{T_{c1}}Q_{c1} + \frac{T_{c3}}{T_{c2}}Q_{c2} + Q_{c3}, \tag{27}$$

which represents the performance of the system when Q_{c1} and Q_{c2} are completely converted into cooling capacities at T_{c3} under the ideal condition.

Figure 9 shows the variations of Q_{g1}, Q_{g2}, Q_{g3}, and Q_t with p_s, respectively, when the input acoustic powers are kept constant. For the first two stages, Q_{g1} and Q_{g2} increase monotonically with the increasing p_s. But in the third stage,

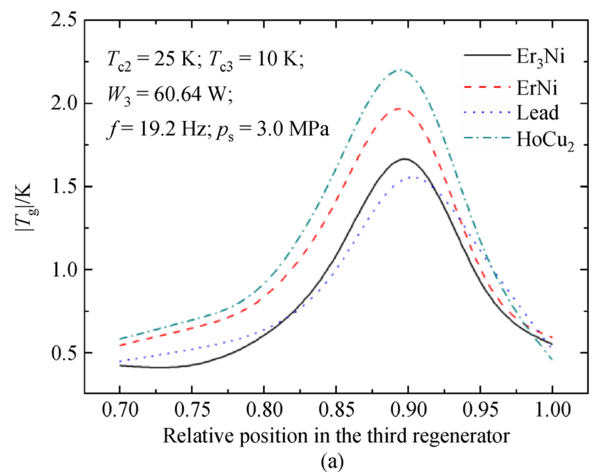

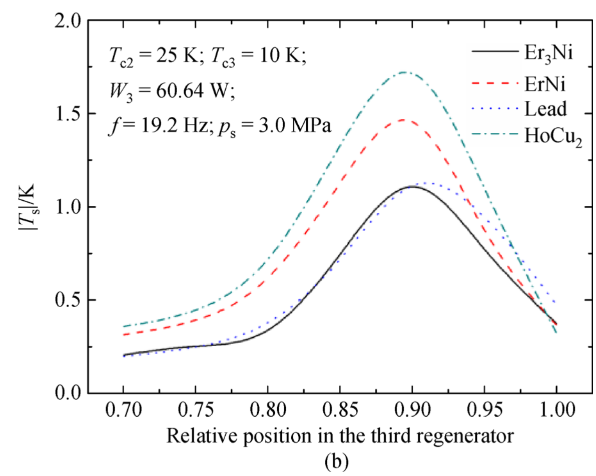

Fig. 7 Influences of different matrices on (a) $|T_g|$ and (b) $|T_s|$ between 10 K and 25 K in the third regenerator

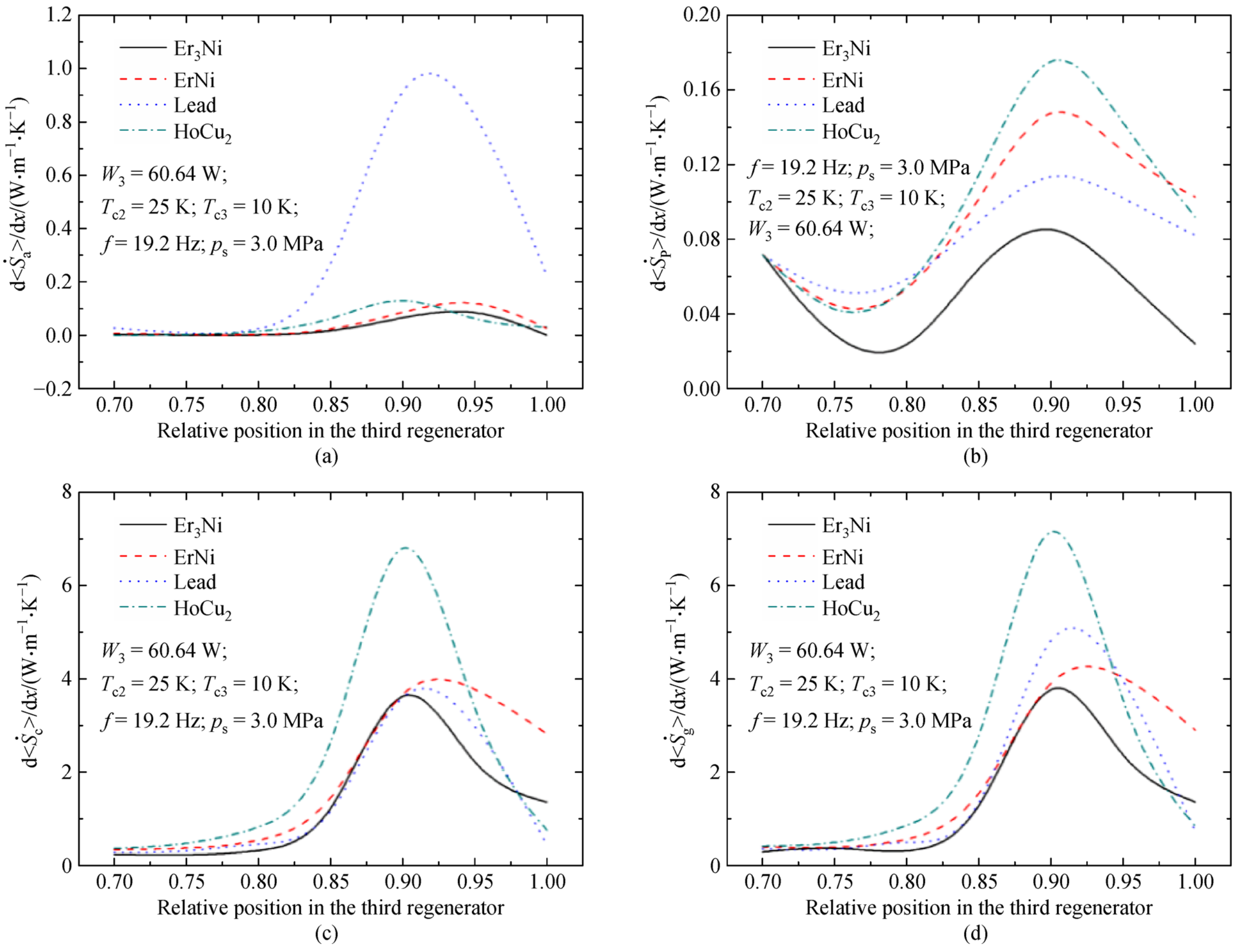

Fig. 8 Influences of different matrices on (a) $<\dot{S}_a>$, (b) $<\dot{S}_p>$, (c) $<\dot{S}_c>$, and (d) $<\dot{S}_g>$ between 10 K and 25 K in the third regenerator

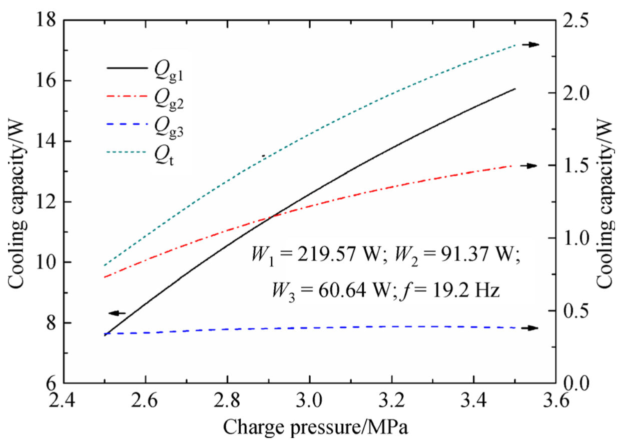

Fig. 9 Effects of charge pressure on Q_{g1}, Q_{g2}, Q_{g3} and Q_t, respectively

Q_{g3} first increases and then decreases, and the largest Q_{g3} occurs when p_s is 3.24 MPa. For the whole system, Q_t is in proportion to p_s, which indicates that a higher charge pressure contributes to improving the total cooling capacity.

Figure 10 shows the influences of the pressure ratio at the inlet on Q_{g1}, Q_{g2}, Q_{g3}, and Q_t, respectively. The variation tendencies of the four curves show that there is a close similarity, that is, the cooling capacity increases monotonically with the increasing pressure ratio. Therefore, an efficient method to optimize the system is to

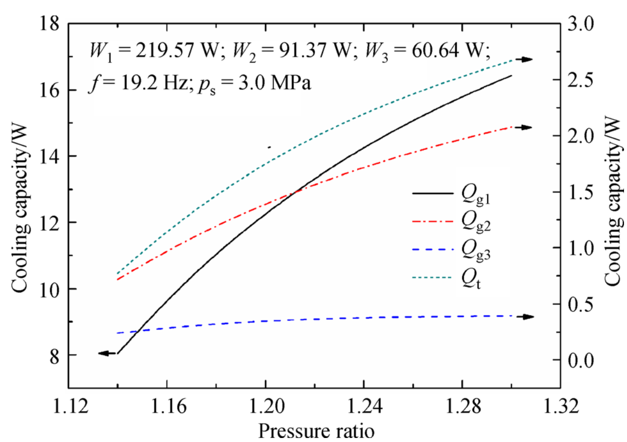

Fig. 10 Effects of pressure ratio on Q_{g1}, Q_{g2}, Q_{g3} and Q_t, respectively

enhance the pressure ratio as high as possible. But it should be noted that the pressure ratio is limited by the used compressor and thus cannot be increased unlimitedly.

3.3 Effect of operating frequency

A basic feature of the SCD three-stage SPTC is that the operating frequency remains the same for all stages, which is fundamentally different from that of its MCD counterpart. Therefore, the optimization of the frequency will affect all stages simultaneously. Figure 11 shows the effects of the frequency on Q_{g1}, Q_{g2}, Q_{g3}, and Q_t, respectively. For each stage, there exists an optimal frequency corresponding to the largest gross cooling capacity, which turns out to be 24.9 Hz, 22.1 Hz and 17.8 Hz, respectively. Generally, the optimal frequency gradually decreases when the stage becomes lower. In consideration of the performance of all of the three stages, in order to achieve the largest Q_t, the optimal frequency becomes 19.2 Hz according to the optimal Q_t.

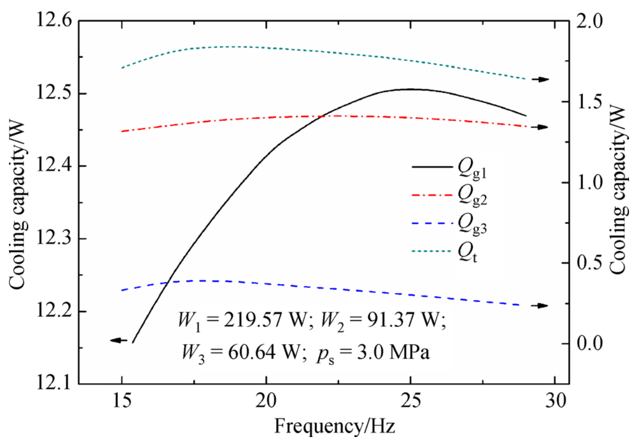

Fig. 11 Effects of operating frequency on Q_{g1}, Q_{g2}, Q_{g3} and Q_t, respectively

4 Experimental verifications

4.1 Experimental set-up

The cold fingers of the developed SCD three-stage SPTC is shown in Fig. 12. Each thermal link consists of 30 pieces of sleet copper with either end welded together. Figure 13 shows the experimental setup, in which the power meter monitors the input voltage, the current, and the electric power while the AC power drives the linear compressor. The temperatures and the cooling capacities of the three stages are measured by the temperature sensors and heaters. A multi-channel DAQ collects the data which are then processed by a computer. The vacuum pump connecting to the dewar is used to ensure the required vacuum environment.

4.2 Comparisons between simulated and experimental results of SCD SPTCs

Based on the above analyses, the optimal values of the key operating parameters such as matrix, charge pressure, pressure ratio, and operating frequency can be obtained, and the cooling performance of the SCD three-stage SPTC can be worked out quantitatively.

Both the simulated and experimental results are shown in Fig. 14. With a total input acoustic power of 371.58 W, the developed SCD three-stage SPTC can experimentally obtain cooling capacities of 2.4 W at 70 K, 0.17 W at 25 K, and 0.05 W at 10 K simultaneously. There is a good agreement between the simulated and experimental results of the cooling capacities of the third stage. The no-load temperatures of the simulated results and the experimental ones are 7.8 K and 8.82 K, respectively.

4.3 Comparisons between SCD and MCD SPTCs in experiments

The MCD three-stage SPTC reported by the laboratory could achieve a no-load temperature of 6.82 K with a total input power of 370 W [18–20]. In Fig. 15, given the same input power, the no-load temperature of the SCD three-stage SPTC reaches 8.82 K and the cooling capacity is slightly poorer than that of its MCD counterpart, which indicates that the great advantages such as compactness and lightweight of the former also involve some sacrifices of the cooling efficiency of the system.

5 Conclusions

A theoretical model of the SCD three-stage SPTC is established and an in-depth analysis of it is conducted in this paper. The main differences between the SCD and the MCD types are expounded, such as the distribution of the input acoustic power in each stage, and the optimization of the operating parameters, in which both advantages and difficulties of the former are stressed. The effects of dynamic temperatures are considered to improve the accuracy at very low temperatures. The effects of dynamic temperatures are considered to improve the accuracy at very low temperatures. A specific example aiming at 10 K is given to provide quantitative analyses and comparisons, from which some meaningful conclusions are reached.

(1) Dynamic temperatures of the gas and the matrix can be ignored in the first stage, but they have significant influences on the internal flows of the last two stages. Besides, the amplitudes of dynamic temperatures of the gas and the matrix, i.e., $|T_g|$ and $|T_s|$, increase monotonically with the decreasing temperature in both ranges of 300–70 K and 70–25 K. However, between 10 K and 25 K, both $|T_g|$ and $|T_s|$ first increase and then decrease. In addition,

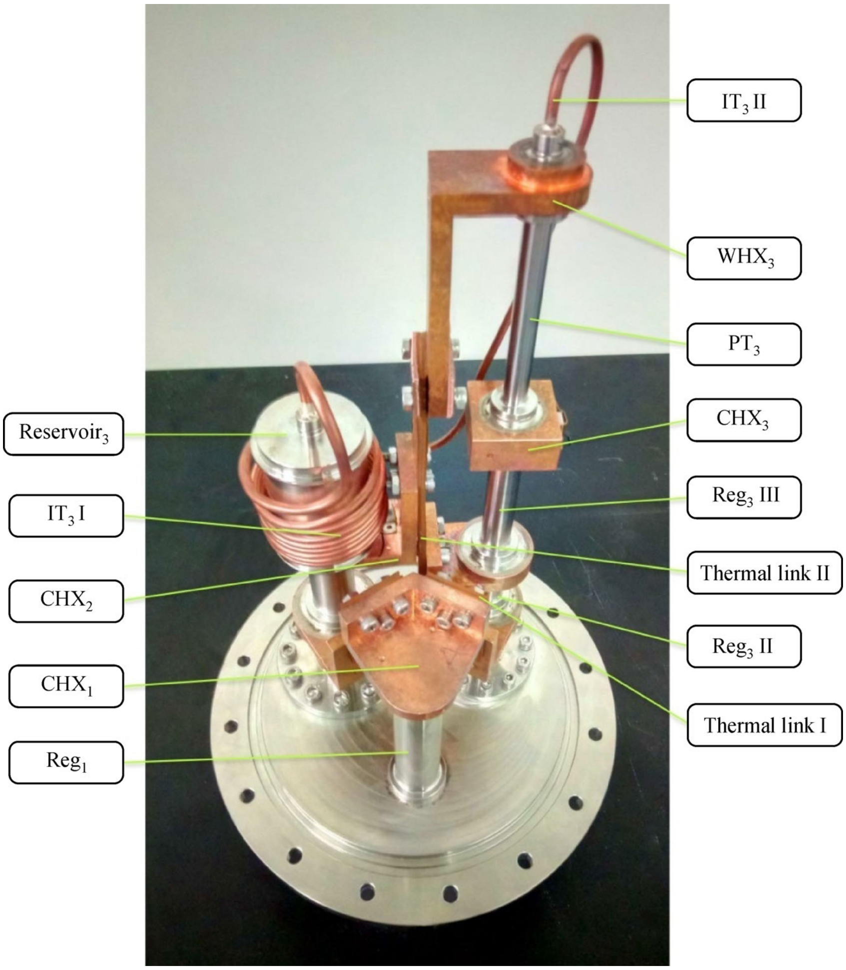

Fig. 12 Cold fingers of the developed SCD SPTC

the phase difference between the two dynamic temperatures, i.e., θ_{gs}, decreases monotonically with the decreasing temperature all the time.

(2) The distribution of the input acoustic power is determined by the impedance of each stage. Its expressions are worked out based on a further improved ECA model. Generally, for the lower stage, the regenerator is longer and thinner, which may result in a larger resistance, and thus the input acoustic power is normally smaller than that of upper stages.

(3) The simulation results of the optimizations of the SCD three-stage SPTC indicate that Er_3Ni is the best matrix between 10 K and 25 K, followed by ErNi, Pb, and $HoCu_2$. Besides, a higher charge pressure contributes to the enhancement of the total cooling capacity of the three-stage SPTC. Moreover, to increase of the pressure ratio as high as possible is also an efficient method to improve the performance of the overall system. Furthermore, there exists an optimal frequency corresponding to the largest total cooling capacity, which turns out to be 19.2 Hz for the given example.

(4) With a total input power of 371.58 W, the developed SCD three-stage SPTC can reach a no-load temperature of 8.82 K and experimentally achieve the cooling capacities of 2.4 W at 70 K, 0.17 W at 25 K, and 0.05 W at 10 K simultaneously, which is slightly poorer than those of its MCD counterpart. The results indicate that the great advantages such as compactness and lightweight of the former also involve some sacrifices of the cooling efficiency of the system.

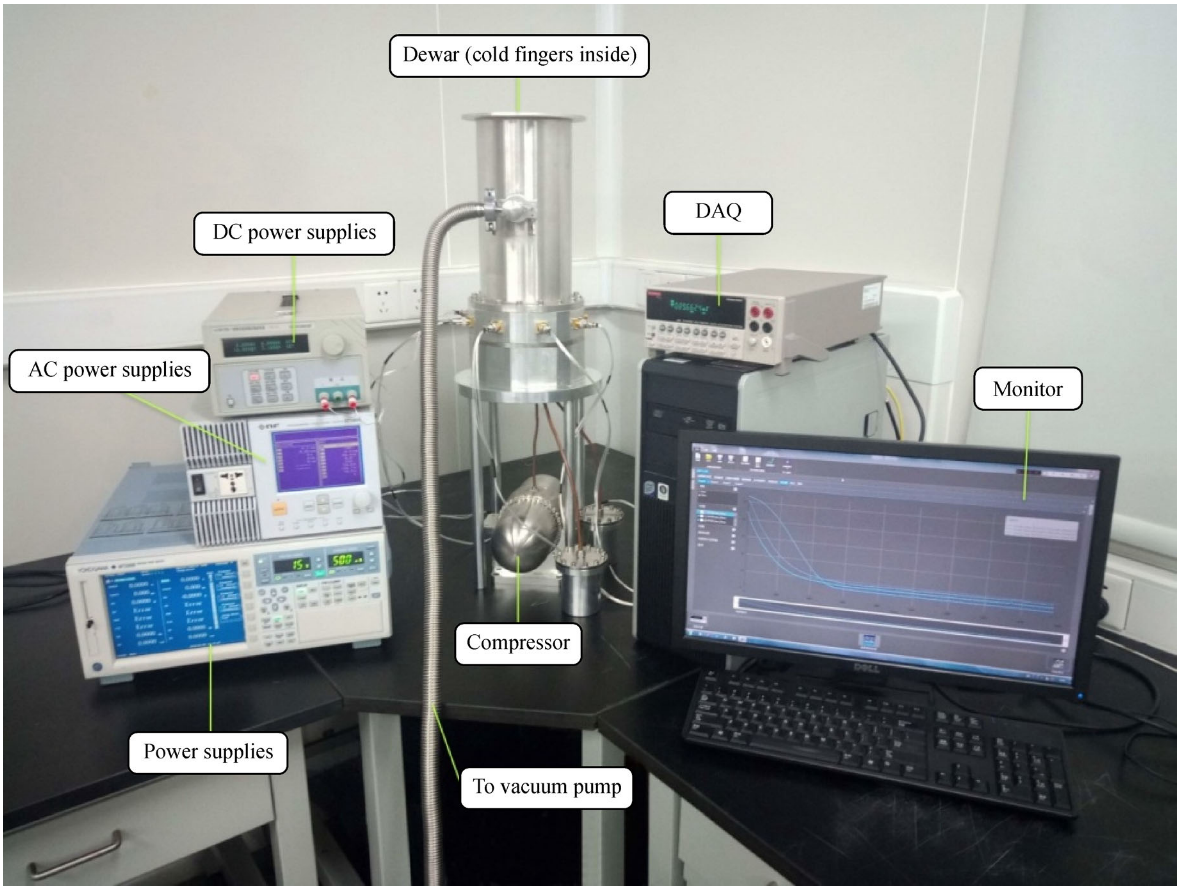

Fig. 13 Experimental setup

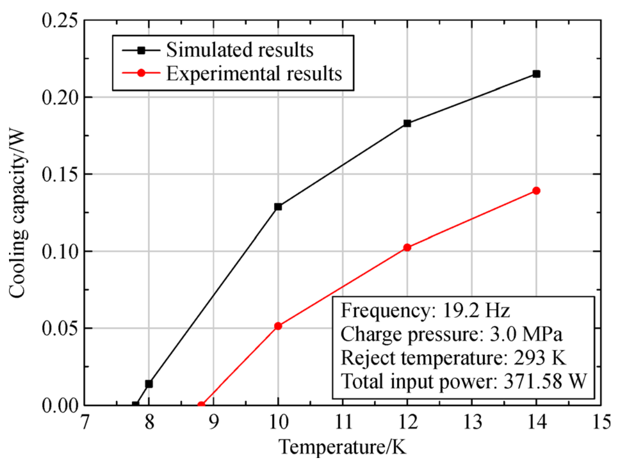

Fig. 14 Comparisons of simulated and experimental results

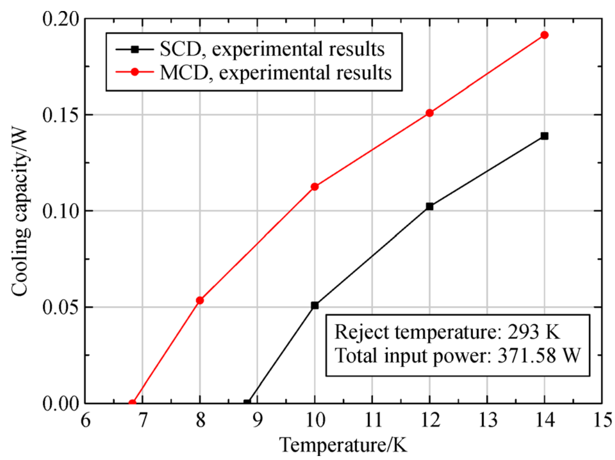

Fig. 15 Comparisons of experimental results between SCD and MCD SPTCs

Acknowledgements The work was financially supported by the Aeronautical Science Foundation of China (Grant No. 20162490005), and the Science and Technology Commission of Shanghai Municipality (Grant No. 18511110100).

Notations

A	Area/m^2
c	Specific heat/($\mathrm{J \cdot kg^{-1} \cdot K^{-1}}$)
C_f	Compressibility factor

E	Ratio of dynamic temperature between gas and matrix
f	Frequency/Hz
F	New defined parameter (kg/m·s^2)
g	Variation coefficient for volume flow rate caused by temperature gradient/m^{-1}
h_{gs}	Convective heat transfer coefficient between gas and solid/(W·m^{-2}·K^{-1})
H	Enthalpy flow/J
p	Pressure/Pa
p_d	Dynamic pressure/Pa
p_s	Charge pressure/Pa
Q	Heat/W
Q_c	Cooling capacity/W
Q_g	Gross cooling capacity/W
Q_p	Precooling capacity/W
Q_t	Total cooling capacity/W
r_g	Flow resistance per unit length/(kg·m^{-5}·s^{-1})
r_h	Hydraulic radius/m
R	Ideal gas constant/(J· kg^{-1}·K^{-1})
R_v	Viscous resistance/(kg·s^{-4}·s^{-1})
S	Entropy/(J·K^{-1})
S_g	Entropy generation/(J·K^{-1})
t	Time/s
T	Temperature/K
u	Gas velocity/(m·s^{-1})
$\dot{U}$	Volume flow rate/(m^3·s^{-1})
W	Acoustic power/W

Greek symbols

β	Specific surface area/m^{-1}
γ	Specific heat ratio
δ_v	Viscous penetration depth/m
η	Heat conduction efficiency
θ	Angle/rad
λ	Thermal conductivity/(W·m^{-1}·K^{-1})
μ	Viscosity/(Pa·s)
φ	Porosity
Π	Perimeter/m
ρ	Density/(kg·m^{-3})
ω	angular frequency/(rad·s^{-1})

Subscripts

c	Cold end of the regenerator
g	Gas
h	Hot end of the regenerator
i	Inner part
m	Mean value
s	Solid
w	Wall

References

1. Jr Ross R G. Aerospace coolers: a 50-year quest for long-life cryogenic cooling in space. In: Timmerhaus K D, Reed R P, eds. Cryogenic Engineering: Fifty Years of Progress. New York: Springer Publishers, 2006, 225–284
2. Dang H Z. Development of high performance moving-coil linear compressors for space Stirling-type pulse tube cryocoolers. Cryogenics, 2015, 68: 1–18
3. Wilson K B, Gedeon D R. Status of pulse tube cryocooler development at Sunpower. Cryocoolers, 2005, 13: 31–40
4. Olson J, Nast T C, Evtimov B, Roth E. Development of a 10 K pulse tube cryocoolerfor space applications. Cryocoolers, 2003, 12: 241–246
5. Olson J R, Moore M, Champagne P, et al. Development of a space-type 4-stage pulse tube cryocooler for very low temperature. Advances in Cryogenic Engineering, 2006, 51: 623–631
6. Raab J, Colbert R, Harvey D, et al. NGST advanced cryocooler technology development program (ACTDP) cooler system. Cryocoolers, 2005, 13: 9–14
7. Bradley P E, Radebaugh R, Garaway I, et al. Progress in the development and performance of a high frequency 4 K Stirling-type pulse tube cryocooler. Cryocoolers, 2011, 16: 27–33
8. Duval J M, Charles I, Butterworth J, et al. 7 K–15 K pulse tube cooler for space. Cryocoolers, 2013, 17: 17–23
9. Gao Z Q, Dang H Z. Entropy analyses of the three-stage thermally-coupled Stirling-type pulse tube cryocooler. Applied Thermal Engineering, 2016, 100: 944–960
10. Xu M Y, de Waele A T A M, Ju Y L. A pulse tube refrigerator below 2 K. Cryogenics, 1999, 39(10): 865–869
11. Ju Y L. Thermodynamic analysis of GM-type pulse tube coolers. Cryogenics, 2001, 41(7): 513–520
12. Kittel P. Enthalpy, entropy, and exergy flows in pulse tube cryocoolers. Cryocoolers, 2005, 13: 343–352
13. He Y L, Huang J, Zhao C F, Liu Y W. First and second law analysis of pulse tube refrigerator. Applied Thermal Engineering, 2006, 26 (17–18): 2301–2307
14. Yuan S W K, Curran D G T. A new load-shifting concept for multistage cryocoolers. Cryocoolers, 2009, 15: 89–96
15. Wang C A. 4 K pulse tube cryocooler with large cooling capacity. Cryocoolers, 2016, 19: 299–305
16. Tan J, Dang H Z. An electrical circuit analogy model for analyses and optimizations of the Stirling-type pulse tube cryocooler. Cryogenics, 2015, 71: 18–29
17. Dang H Z, Zhang L, Tan J. Dynamic and thermodynamic characteristics of the moving-coil linear compressor for the pulse tube cryocooler. Part A: Theoretical analyses and modeling. International Journal of Refrigeration, 2016, 69: 480–496
18. Gao Z Q, Dang H Z, Bao D L, Zhao Y B. Investigation on a three-stage Stirling-type pulse tube cryocooler for cooling the low-T_c SQUID. IEEE Transactions on Applied Superconductivity, 2017, 27 (4): 1601405
19. Dang H Z, Tan J, Zha R, et al. Advances in single- and multi-stage Stirling-type pulse tube cryocoolers for space applications in NLIP/

SITP/CAS. IOP Conference Series: Materials Science and Engineering, 2017, 278: 012008
20. Dang H Z, Bao D L, Zhang T, et al. Theoretical and experimental investigations on the three-stage Stirling-type pulse tube crycooler using cryogenic phase-shifting approach and mixed regenerator matrices. Cryogenics, 2018, 93: 7–16